

Efficient 3D Reconstruction of Vessels from Multi-views of X-Ray Angiography

Anonymous submission

Abstract

In this paper, we present an efficient 3D vessels reconstruction algorithm based on multi-views of X-ray Angiography assisting interventional surgery. First, we extract the vascular-like structures from the image sequences using a geometrical analysis of multi-scale Hessian matrix eigen-system and use the fast marching method to extract the skeleton of the structure, from which we derive the vascular topological configurations. Second, we regard the 3D space as a Markov Random Field and formulate the reconstruction problem as an energy minimization problem with consistent, continuous and topological constraints to coarsely register and reconstruct the 3D vessels. Third, we refine the reconstructed vessels to register and reconstruct the 3D vessels accurately. We demonstrate our system in coronary arteries reconstruction for percutaneous coronary intervention surgery to help doctors learn about the configurations of the coronary arteries of specific patient during operation. We envision that our system will be used for clinic treatment to advance vessel reconstruction for diagnosis and therapy in the near future.

Keywords: X-Ray angiography, 3D reconstruction, Multi-scale retinex, Belief propagation

1. Introduction

Intraoperative X-Ray is essential during some surgeries, such as percutaneous coronary intervention. The 2D X-Ray images not only lose a significant amount of 3D information of the coronary arteries, but also suffer from the viewing angle dependence, magnification factor, overlapping and the blurring between vessels, backgrounds and other tissues and organs.

Great efforts have been done on 3D reconstruction of coronary arteries to overcome the shortcomings of 2D images. But there are also some problems existing in current methods. First, the absence of image enhancement procedures may lead to disappearance of some tiny details because of the low contrast and blurring of angiograms. Second, the vessel skeleton extraction methods are not accurate and may acquire discontinuous or unsmooth results. Third, accurate reconstructions need five or more views of angiograms with exact angle requirements, which is hard to operate for clinical use. Fourth, current 3D reconstruction methods mostly rely on the registrations between image pairs, which are hard to add constrain conditions such as consistency and continuity.

To overcome these shortcomings, we present an efficient vessel reconstruction system from multiple X-Ray views. The pipeline is shown in Figure 1. First, we apply the multi-scale retinex method to enhance the con-

28 trast of the angiogram. Second, we implement a CU-
29 DA edition of Hessian matrix based vessel filter with
30 hysteresis thresholding to get the preprocessing results.
31 Third, we perform the fast-marching method using sec-
32 ond order derivatives and cross neighbor templates to
33 extract the accurate centerline of the vascular-structure.
34 Finally, 3D reconstruction with local constraints and s-
35 pace consistencies is formulated as an energy minimiza-
36 tion problem and solved using belief propagation. All
37 these lead to a fast reconstruction result of the data and
38 promise accuracy and efficiency which can give the doc-
39 tor a good sense of coronary artery 3D space structures.
40 The contributions of the paper are:

41 (1) We combine the MSR enhanced images which
42 are mostly over extracted with line segments tracking
43 methods to obtain more detailed vessels from blurry an-
44 giograms.

45 (2) We divide the spaces between the X-Ray iso-
46 center and the detector into slices in which we sample
47 the 3D space points and project them to the image s-
48 pace considering consistency and continuity with their
49 neighbors, overcoming the lack of constraints for typi-
50 cal registrations.

51 (3) We formulate the 3D reconstruction as a global
52 energy optimization problem and solve it by using belief
53 propagation.

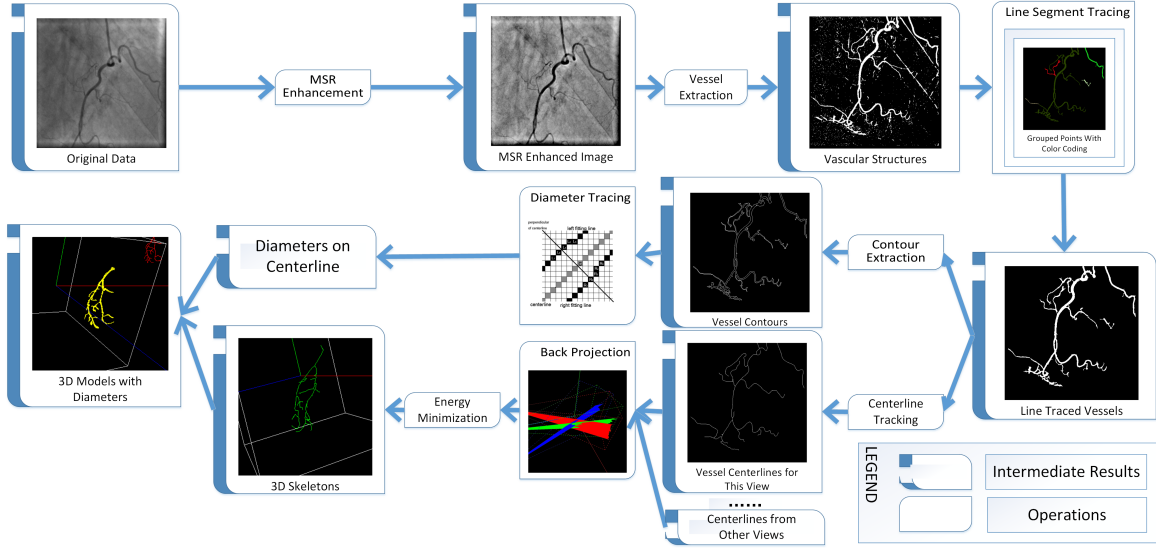


Figure 1: Work Pipelines

54 2. Related Work

55 Our work relates to vessel extraction from image and
 56 vessel reconstruction etc. We briefly review them in the
 57 following categories.

58 *Vessel Extraction*

59 Hoover et al. [1] use a mathematical filter to entails
 60 a broad range of vessel enhancement and Li et al. [2]
 61 do this using a non-linear filter. Frangi et al. [3] use the
 62 eigen values of Hessian matrix to extract the tube-like
 63 structures from the X-Ray images. Condurache et al. [4]
 64 use this method while adding a hysteresis thresholding
 65 method to purify the extracted data.

66 *Centerline Extraction*

67 Centerline extraction consists of six kinds of tech-
 68 niques: pattern recognition techniques, deformable
 69 model based techniques [5][6][7], tracking-based tech-
 70 niques [8][9][10] [11] [12], artificial intelligence-based
 71 techniques, neural network-based techniques and mis-
 72 cellaneous tube-like object detection techniques. Each
 73 one contains many sub-types such as multi-scale ap-
 74 proaches, mathematical morphology approaches. Read-
 75 ers please refer to [13] for an overview of the centerline
 76 extraction technologies.

77 *3D Reconstruction*

78 As with 3D reconstruction, Wellnhofer et al. [14] and
 79 Messanger et al. [15] evaluate that 3D reconstructions
 80 of coronary arteries from 2D X-Ray image sequences

81 permit accurate results of the real data. The two type-
 82 s of the X-Ray machine lead to two slightly different
 83 ways of 3D reconstruction. The biplane system takes
 84 two (mostly) synchronized projection of the coronary
 85 arteries [14][15]. Meanwhile the mono-plane (single-
 86 plane) system [16] can just take one view at the same
 87 time, therefore selection of asynchronous images from
 88 multiple views is needed. However, using only two
 89 2D projections to reconstruct the complex 3D topo-
 90 gy of coronary artery is often not sufficient. Movas-
 91 saghi et al. [17] uses multiple projections for realistic
 92 vessel lumen simulations, but only uses two for 3D cen-
 93 terline reconstruction. Sprague et al. [18] utilizes the
 94 benefits of three projections experimentally. Hansis et
 95 al. [19] has used multiple projections from a single ro-
 96 tational X-Ray angiography to reconstruct the 3D cen-
 97 terline and the topology. Nguyen et al. [20] propose
 98 a method based on motion and multiple views using a
 99 single-plane imaging system. They only consider the
 100 rotation and scaling of the heart motion but rigorously
 101 the heart motion during contraction and relaxation con-
 102 sists of five movements: translation, rotation, wringing,
 103 accordion-like motion and movement towards the cen-
 104 ter of the ventricular chamber [21]. Therefore, a simple
 105 motion can not generally describe the heart cardiac cy-
 106 cle.

107 Other routines such as knowledge-based or rule-
 108 based have been proposed for 3D reconstruction using
 109 the vascular network model [22] [23]. Since their rules
 110 or knowledge are designed for specific conditions, it is
 111 not easy to generalize these kinds of methods to process

112 artery data.

113 In [24][25][26], optimal estimation are investigated
114 with a two-step approach based on maximum-likelihood
115 and minimum-variance estimation. They use a linear al-
116 gorithm to compute the preliminary estimates as the ini-
117 tial estimates for the process of optimal estimation. Due
118 to the huge computation, none of the existing techniques
119 have been used in clinical therapy.

120 Other Focuses

121 Another focus on 3D reconstruction is on the elim-
122 ination or minimization of foreshortening and overlap
123 of the coronary arteries which is a prerequisite for an
124 accurate quantitative coronary analysis such as the ves-
125 sel lengths and aneurysms. In [27], they focus on the
126 minimization of vessel foreshortening relative to a sin-
127 gle arterial segment. Sato et al. [28] and Finet et al. [29]
128 introduce an optimal view selection method considering
129 both foreshortening and vessel overlap. Chen et al. [30]
130 use bifurcation points and the vessel directional vectors
131 of bifurcations to register between image pairs. Mean-
132 while, they also proposed a method of selecting the min-
133 imized foreshortening views. But, it depends on bifur-
134 cations overmuch and requires at least five pairs of bi-
135 furcations to ensure accurate transformation. Also, their
136 work is time consuming with a whole procedure of ten
137 minutes.

138 3. Methods

139 3.1. Data Acquisition and Preprocessing

140 3.1.1. Data Acquisition

141 For all procedures, we use two types of data. One is
142 the synthetic data from our simulation system described
143 in Figure 2 with vessel trees' ground truth known. The
144 other one is the real data from the clinical angiogram.

145 For simulation data, we use three different views re-
146 spectively at RAO 50, LAO 50, LAO 0, while at the
147 same CRA angle. For real data, we use LAO 2, CRA 29
148 as the middle view, and LAO 32, CRA 27 as the left ref-
149 erence view, and RAO 25 CRA 29 as the right view. All
150 the sequences of the views consist at least 50 images
151 with the pixel resolution of 512×512 . We select one
152 image from each view at the mostly the same cardiac
153 cycle and use them to reconstruct the vessels.

154 3.1.2. Multiscale Retinex Image Enhancement

155 The original angiograms acquired from the X-Ray
156 machine have many shortcomings such as the low image
157 contrast, the low lumen with the wide dynamic range.
158 Current methods for X-Ray angiograms enhancement

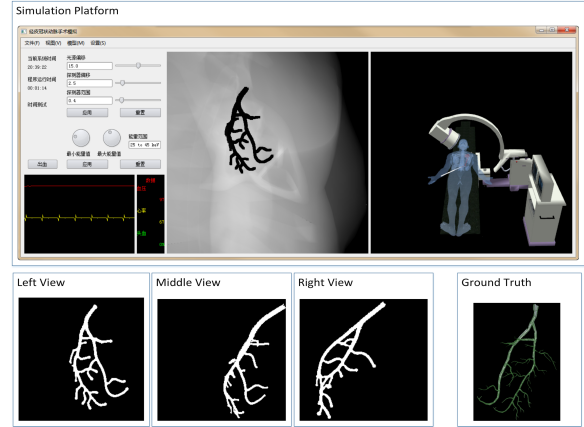


Figure 2: Our Simulation Platform

159 such as gain/offset fix, histogram equalization can only
160 work well for specific angiograms. Take histogram e-
161 qualization for example, it can only handle images with
162 one single apex, while for double or several apexes, sat-
163 isfactory results can not be achieved. In our approach,
164 we apply an enhancement of radiography based on Mul-
165 tiscale Retinex.

166 Land et al. [31] first proposed the Retinex as a model
167 for human perception of brightness and color and for-
168 mulates the ideal images as

$$f(x, y) = r(x, y) \times i(x, y) \quad (1)$$

169 where $i(x, y)$ is the environment brightness function
170 which describes the brightness of the surroundings,
171 while the $r(x, y)$ is the scene reflection function which
172 describes the ability of the scene to reflect itself. Jobson
173 et al. [32] defined the single retinex algorithm which can
174 be described as

$$R(x, y) = \log I(x, y) - \log [F(x, y) * I(x, y)] \quad (2)$$

175 where $R(x, y)$ is the output image, $I(x, y)$ is the input
176 image, $*$ stands for convolution, \log is the natural log,
177 $F(x, y)$ is the environment function. Moore [33] pro-
178 posed to use the

$$F(x, y) = \exp(-r/c) \quad (3)$$

179 A better approach for this function is the Hurlbert's
180 [34] work, they define $F(x, y)$ as

$$F(x, y) = K \exp(-(x^2 + y^2)/\sigma^2) \quad (4)$$

181 where σ is the standard deviation of gaussian func-
182 tion which controls the detail preservation, K should af-
183 ford

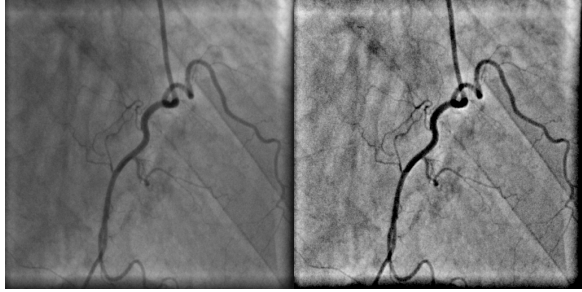


Figure 3: Left: Original Image, Right: Enhanced Image

$$\iint f(x, y) dx dy = 1 \quad (5)$$

Single Retinex can not achieve good results both on color consistency and dynamic range compression. We use the method based on Multiscale Retinex(MSR) which can be described as

$$R_i = \sum_{k=1}^K W_k (\log I_i(x, y) - \log [F_k(x, y) * I_i(x, y)]) \quad (6)$$

where i stands for the i th channel, K stands for the channel number, W_k and F_k are the weight coefficients. After MSR, we use the gain/offset method to fix the negative values of the image

$$R_o(x, y) = G \times R_i(x, y) + offset \quad (7)$$

$$R(x, y) = 255 \times \frac{R_o(x, y) - r_{min}}{r_{max} - r_{min}} \quad (8)$$

where $R_i(x, y)$ and $R_o(x, y)$ are the image input and output, $R(x, y)$ is the final grey image.

In our approach, we use four different Gaussian filter coefficients under four different deviations were calculated. Then we apply a convolution between the original images and the Gaussian filters and get a weighted average result of the four different filters. After all these, the X-Ray angiograms are obviously enhanced with higher contrast and low dynamic ranges shown in Figure 3.

3.2. Vessel Extraction

3.2.1. Vessel extraction based on Hessian matrix

For vessel extraction on X-Ray angiograms, vessels are often hard to be sensed due to the low intensity contrast as well as their soft issues. Even for fine vascular structures, this problem is severe. The major challenge relies on how to enhance or extract the vascular structure with the avascular as less as possible.

After achieving the high-contrast images preprocessed by MSR, we use the approach proposed by [3]. It relies on a multiscale Hessian matrix that enhances the vascular structures.

Hessian matrix considers the local features of the vessels. A common approach to analyze the local features of a 2D/3D image is to consider the Taylor expansion in the neighborhood of a point x_0

$$I(x_0 + \Delta x) \approx I(x_0) + \Delta x^T \nabla I(x_0) + \Delta x^T H(x_0) \Delta x \quad (9)$$

where ∇I is the gradient vector and H donates the Hessian matrix- which is the second-order partial derivatives of I

$$H = \begin{pmatrix} I_{xx} & I_{xy} \\ I_{yx} & I_{yy} \end{pmatrix} \quad (10)$$

For a given scale σ , the image I is first convoluted with a 2D Gaussian filter G_σ . The convoluted image can be explained by $I_\sigma = I * G_\sigma$. The Hessian matrix of the convoluted image can be computed by

$$HI_\sigma = \begin{pmatrix} \frac{\partial^2 I_\sigma}{\partial x^2} & \frac{\partial^2 I_\sigma}{\partial y \partial x} \\ \frac{\partial^2 I_\sigma}{\partial x \partial y} & \frac{\partial^2 I_\sigma}{\partial y^2} \end{pmatrix} \quad (11)$$

The eigenvalues and eigenvectors of the Hessian can be used to extract the features of the local structures. The direction of the potential locally rectilinear structure can be calculated by

$$\tan(2D_\sigma) = 2 \frac{\partial^2 I_\sigma}{\partial y \partial x} \left(\frac{\partial^2 I_\sigma}{\partial x^2} - \frac{\partial^2 I_\sigma}{\partial y^2} \right) \quad (12)$$

For coronary arteries, their sizes are varied and particularly tiny. In our experiments, we use the interval [0.3 3] with the step 0.3 to get ten representations of the original images. Then, for every pixel on the image, we calculate the second-order derivatives to build the Hessian matrix H . Next, before eigenvalues decomposition, we normalize the Hessian matrix which is divided by σ^2 . After the normalization, we decompose the Hessian matrix into its corresponding eigenvalues λ_1, λ_2 , here we assume $|\lambda_2| \ll |\lambda_1|$. According to [3], we define parameters by

$$R_b = \frac{\lambda_2}{\lambda_1} \quad (13)$$

which attains its maximum for a blob-like structure and is zero whenever $\lambda_2 \approx 0$, or λ_1 and λ_2 tend to vanish.

$$S^2 = \lambda_1^2 + \lambda_2^2 \quad (14)$$

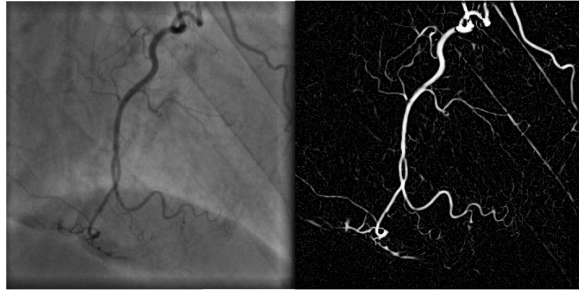


Figure 4: Possibility Image

which is used to distinguish plate-like(non-zero) and line-like (zero) structures. Finally, we get the equation specifying the possibility of a pixel being one part of vessel structures

$$v_\sigma(s) = \begin{cases} 0, & \text{if } \lambda_1 < 0, \\ \exp(-\frac{R_b^2}{2\beta^2})(1 - \exp(-\frac{s^2}{2c^2})), & \text{else} \end{cases} \quad (15)$$

where β and c are parameters that control the sensitivity and continuity of the filter.

Finally, having performed the same process on all the other scales, the scale with maxima v_σ is selected and the corresponding value is recorded. This value can be regarded as the possibility of the vascular structures' occurrence at this position. We initialize a new image with the same size as the original image using Hysteresis Thresholding. The pixel values of the image are the corresponding values of the recorded values ranging from 0 to 1. The extraction result are shown in Figure 4.

After having got the possibility image, we initialize another new binary image for calculating centerlines. The pixels where the extraction values are greater than zero are white while the others are black. We compute the connectivity of the whole image using a cross template so that line segments whose length are smaller than a typical value are regarded as noise as well as many noisy points produced by enhancement during M-SR. After all these steps, we can reduce over-extraction and noise as much as possible. The tracking result is shown in Figure 5.

3.2.2. Hysteresis-like Thresholding

Hysteresis thresholding is to discard obvious non-vascular structures from the result images while retaining the definite values. We use a histogram of the image grey values to compute the quantiles of them as the basis of thresholds. The low threshold is chosen low enough to obtain a slightly over detection.

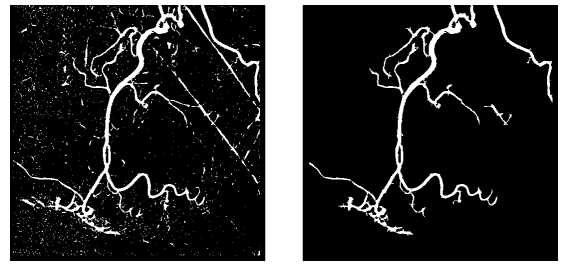


Figure 5: Line Segment Trace Image

3.3. Centerline Tracking

After getting the binary images of the vascular structures, we apply the centerline extraction method using fast marching based on Hassouna [35]'s and Jakob [36]'s work. They use fast marching method to obtain an accurate solution of Eikonal equation known as

$$|\nabla T|F = 1, \text{ s.t. } T(\Gamma_0) = 0$$

where Γ stands for the closed interface that separates one region from another. Hassouna et al. [35] proposed an improved version of the fast marching method with high accuracy called multistencils fast marching(MSFM). By solving the Eikonal Equation at each point under several stencils which cover 8 neighbours in 2D space and 26 in 3D space and picking up the one which satisfies the upwind condition most, they can achieve better accuracy. For stencils not aligned with the natural coordinate system, Eikonal equation is derived using directional derivatives and solved using higher finite difference schemes.

Our approach is based on Jakob [36]'s work. The 2D binary image points can be divided into *frozen pixels* which we compute distances at their neighbours and *narrow band* pixels. For each iteration, the *narrow band* pixels having the smallest distance value is frozen and distances are computed from its neighbours. Progressively, the *narrow band* pixels propagate from the initial condition and the freezing pixels follow them along, finally, when all points are frozen, the method vanishes. During the procedure, we use the method proposed as Hassouna [35] to compute the distances and implement a custom unsorted binary tree which performs like a normal binary sorted tree to select the minimum distance in every MSFM iteration.

During the centerline tracking, every point in each line is tracked and the bifurcations are recorded, finally we can get a vessel centerline tree including all bifurcations as shown in Figure 6. The left image is the binary image representing the centerlines of the vessels,

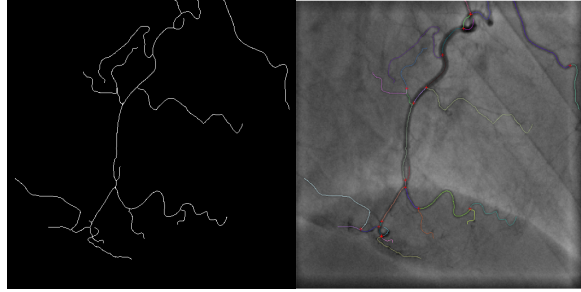


Figure 6: Binary and Colored Centerlines

311 the right is the original image with colored centerlines.
 312 Each red cross represents one bifurcation and each color
 313 represents one single centerline.

314 3.4. Vascular Diameter Extraction

315 The vessel diameter is an important indicator for
 316 many vascular diseases from the X-Ray angiogram and
 317 the precise estimation of vascular centerlines and widths
 318 is very important for the quantitative and visualized di-
 319 agnosis of blood vessel disease. Currently the diagnosis
 320 of the vessel from the angiograms mainly depends on
 321 doctors' naked eyes. The diagnosis results are much af-
 322 fected by human factors and lead to coarse objectivity
 323 and low accuracy.

324 In our approach, we combine the centerlines and the
 325 extracted vascular structures and use the centerlines as
 326 sample bases for diameter computation. Due to the
 327 discreteness of extracted results, we propose a method
 328 based on line fitting to obtain continuous diameters
 329 shown in Figure 7.

330 First, for specified centerline point $C(i, j)$, we get t-
 331 wo adjacent neighbours on both its left and right side.
 332 Using this five points including the point $C(i, j)$, we get
 333 the line L_c crossing the centerline point. Then we can
 334 achieve the perpendicular line's slope at point $C(i, j)$
 335 and compute its intersection point with the vascular
 336 structures contour L_3 and R_3 . With these two points,
 337 we get the forward and backwards two points of the
 338 contour. Then, we get the left intersection group $L =$
 339 $(L_1, L_2, L_3, L_4, L_5)$ and the right $R = (R_1, R_2, R_3, R_4, R_5)$
 340 and the fitting lines L_l and L_r using the point group-
 341 s. At last, we obtain the intersection of $C_L(x_l, y_l)(L_c$
 342 and $L_l)$ and $C_R(x_r, y_r)(L_c$ and $L_r)$. We use the distance
 343 $D = \sqrt{(x_l - x_r)^2 + (y_l - y_r)^2}$ as the vessel diameter at
 344 the right position $C(i, j)$.

345 Using this method, we extract the diameters of Figure
 346 5, which are continuous and with slight waving values.

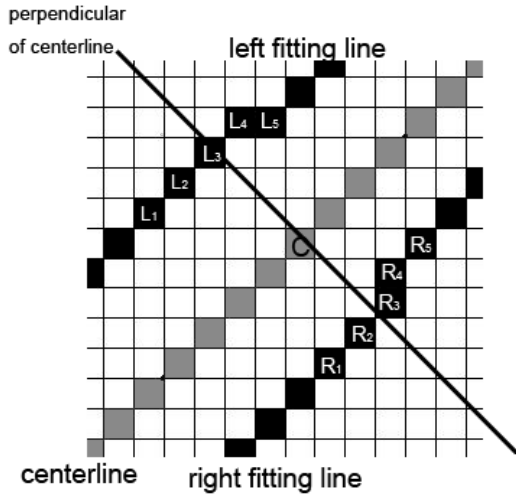


Figure 7: Vessel Diameter Extraction

347 3.5. 3D Reconstruction of Coronary Arteries

348 3.5.1. Reconstruction Overview

349 The angiograms is a procedure of projecting 3D ob-
 350 jects to 2D projection space during which many details
 351 may disappear and foreshorten as well as overlapping.
 352 Just using the 2D projections to justify the patient's con-
 353 ditions has inherent limitations. Using two or several
 354 projections from multi views to reconstruct the topolog-
 355 ical structures of the coronary arteries in 3D space is a
 356 useful method during heart operations such as interven-
 357 ing.

358 The reconstruction of the coronary arteries are re-
 359 garded to the type of the X-Ray machines which can
 360 be divided into single-plane and biplane machines. The
 361 reconstruction based on single-plane angiospasm is to
 362 obtain several angles of views at the same moment of
 363 different cardiac cycles, and uses these projections to
 364 reconstruct the vessels. The difference between the bi-
 365 plane and the single-plane reconstructions is biplane
 366 systems can achieve two synchronous projection pairs
 367 at the same time without time error, leading to less de-
 368 formation of the vessels and high accuracy. For the rea-
 369 son that biplane systems are much more expensive than
 370 single-planes and not common in ordinary hospitals, we
 371 focus on the reconstruction of single-plane systems.

372 In order to reconstruct the 3D vessels, it is importan-
 373 t to find the corresponding points on each angiograms
 374 of different views for all 3D points. In typical methods
 375 registration of the images between different projection
 376 views are needed. However, there are problems they are

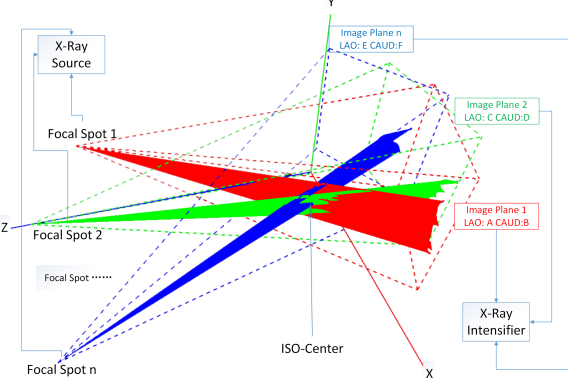


Figure 8: X-Ray Perspective Projection Of Vessel Skeletons

facing. No matter registrations based on features such as bifurcations or any others, the first problem they are facing is that the registration results are mostly not good enough even with many mistakes if the changes among the views are large. The mistakes during registration may lead to much more huge errors during the reconstruction. The second problem is that these kinds of methods are so fixed that neither constraints such as the connectivity of the vessel neighbours nor some known conditions or knowledge can be added which lead to a great waste of the various original information.

3.5.2. Our Method

The imaging modality of the X-Ray angiograms is different from the ways other imaging devices such as cameras or vidicons work in. The light source is the X-Ray source and the imaging plane is the intensifier. The imaging procedure is mostly like perspective projection under 3D space. We simulated this procedure using OpenGL. This can be described in Figure 8

The frustum of each color represents one view of the angiograms. The source of the frustum could be seen as X-Ray source, while the far plane could be seen as the intensifier. The vessel skeletons should be at the iso-center. The exact intersected lines from every view should be 3D space structures of the skeletons of the projected vessels. Being aware of the diameters at every skeleton point, we can get the structures of the vessels.

But the intersections are the correspondence between view pairs. The computation of intersection lines (points) goes back to the registration problem which are ill-posed. Also, due to precision and other errors, it is hard to obtain the accurate intersections among all the views.

However, on the other hand, the 3D skeletons could be regarded as consisting of several skeleton segments.

Each segment could be seen as made up of sampled points. These points must be between the space of the X-Ray source and the intensifier. Also, they should be mostly projected onto every view. So, if we sampled the space between source and intensifier using a tiny enough uniform step, points or their approximations that belong to the skeleton must be inside them. Finally, the problem has transformed into how to extract these points.

In our opinion, each 3D point in the sampled space could be assigned with a probability of being one of the 3D skeleton points. The possibility could be determined by three main causes. The first is how many views this point could be projected onto. The second is the distance from the corresponding projected 2D point on one view to the valid skeleton point on the same view. Also, according to the continuity of the vascular structures, the distance between neighbored points in the same skeleton should affect the possibility.

Finally, the sampled 3D space between the optical center and the intensifier could be regarded as an Markov Random Field and the reconstruction problem could be seen as an energy minimization problem with consistent, continuous and topological constraints.

3.5.3. Our Implementation

In our approach, we use at least three views of angiograms at the same cardiac cycle and choose the projection view I_1 as a reference view which includes the least foreshortening and overlap among all the views. The 3D space is divided into 3D slices which we call 1 layer $L = (l_1, l_2 \dots l_n)$ using a given depth increments which is shown in Figure 9.

Each depth can be assigned with a label l_i . Meanwhile, each skeleton point on reference view I_1 corresponds one projected line from the source to the intensifier through all the layers.

Therefore, for a given pixel p on I_1 , the pair (p, l_i) uniquely identifies a point in 3D space. So, the goal of the 3D reconstruction is to optimally assign an label l_i to each p on the centerline of the reference view I_1 . This problem can be formulated as an energy minimization problem considering connectivity and topological structures. The energy equation could be defined as

$$E(f) = \sum_{p \in P} D_p(f_p) + \lambda \sum_{p, q \in N} V_{p,q}(f_p, f_q) \quad (16)$$

Our goal is to find the minimum $E(f)$ and we use the belief propagation (BP) method to achieve the solution.

In our method, we define the $V_{p,q}(f_p, f_q)$ as the Euclidean distance between point p, q . And we define the

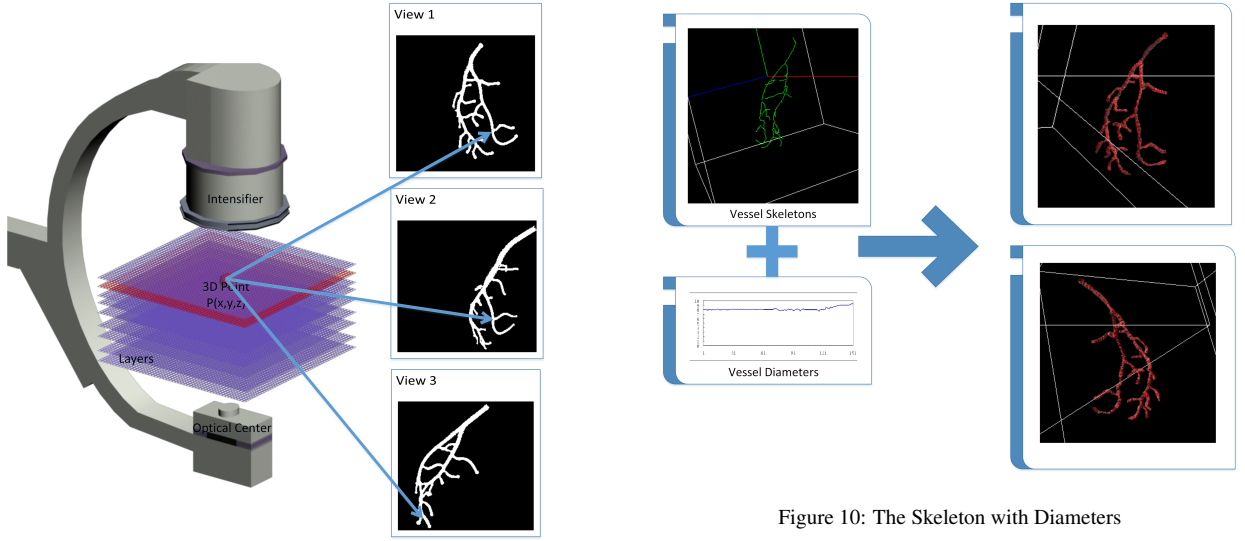


Figure 9: 3D Space Depth Slices

⁴⁵⁹ $D_p(f_p)$ as the *color consistency* which can be described
⁴⁶⁰ as

$$D_p(f_p) = \frac{1}{(n-1)} \sum_{i=2}^n P_i(x, y) \quad (17)$$

⁴⁶¹ where $P_{ith}(x, y)$ is the projection value of point p on
⁴⁶² the ith view, which we define as

$$P_{ith}(x, y) = \begin{cases} W_h, & p(x, y) \in I_{ith} \\ W_l, & \cup(p(x, y), 1) \notin I_{ith} \\ W_a, & \text{else} \end{cases} \quad (18)$$

$$W_a = \frac{1}{N} \sum_{i=1}^N Val_{ith}(x, y) \quad (19)$$

⁴⁶³ where $p(x, y) \in I_{ith}$ means that $p(x, y)$ is a valid cen-
⁴⁶⁴ terline point of I_{ith} , W_h and W_l are two constants that
⁴⁶⁵ control the very high and very low of the value. For a
⁴⁶⁶ grey scale image, $\cup(p(x, y), 1)$ is the 8 neighbors of the
⁴⁶⁷ point $p(x, y)$. If $p(x, y)$ can not be found right in the I_{ith} ,
⁴⁶⁸ we will compute its 8 neighbors and obtain the average
⁴⁶⁹ value as the value of point $p(x, y)$. And if none of its
⁴⁷⁰ neighbors is valid, it could be assigned with W_l .

⁴⁷¹ Our algorithm includes two main steps, message
⁴⁷² propagation and energy minimization computation. In
⁴⁷³ message propagation, the color value of point $p(x, y) \in$
⁴⁷⁴ I_1 is updated as

$$V_p = V_p + \alpha minD + (1 - \alpha)V_{p_{minD}} \quad (20)$$

⁴⁷⁵ where α is a constant controlling the weight its neigh-
⁴⁷⁶ bors' *color consistency* and *dist consistency*. $minD$ s-
⁴⁷⁷ tands for the minimum distance from $p(x, y)$ to its neigh-
⁴⁷⁸ bors. $V_{p_{minD}}$ stands for the value of the minimum dis-
⁴⁷⁹ tance point.

⁴⁸⁰ In our energy minimization, different from typical
⁴⁸¹ BP, the current energy of the ith depth(l_i) is defined as

$$e_i(p_i) = \min[\gamma D(p_i, q) + (1 - \gamma)V(q) + e_{i-1}(q)]; \quad (21)$$

⁴⁸² in which q stands for the projected sample depths of
⁴⁸³ $\cup^o(p_i, 1)$ which is the neighbours of p_i without includ-
⁴⁸⁴ ing p_i itself.

⁴⁸⁵ At last, we compute the minimum sum of all the
⁴⁸⁶ grouped vessel skeletons' cost, and obtain the optimal
⁴⁸⁷ solution for the whole vessel skeleton tree.

⁴⁸⁸ After the reconstruction of the 3D skeletons of the
⁴⁸⁹ coronary arteries, using the diameters we extracted, we
⁴⁹⁰ obtain the final result as shown in Figure 10.

4. Experiments

4.1. Results

⁴⁹³ The reconstruction method was experimented both on
⁴⁹⁴ synthetical data and real clinical data. Compared with
⁴⁹⁵ real data, the reconstruction of synthetical data is easy
⁴⁹⁶ to assess because of knowing the vessel ground truth.
⁴⁹⁷ The final reconstruction results of synthetical data can
⁴⁹⁸ be found in Figure 11.

⁴⁹⁹ In upper columns of Figure 11, the yellow lines indi-
⁵⁰⁰ cate the reconstructed skeleton using our method. The
⁵⁰¹ green lines indicate the ground truth obtained from our
⁵⁰² simulation platform. The white box is the binding box

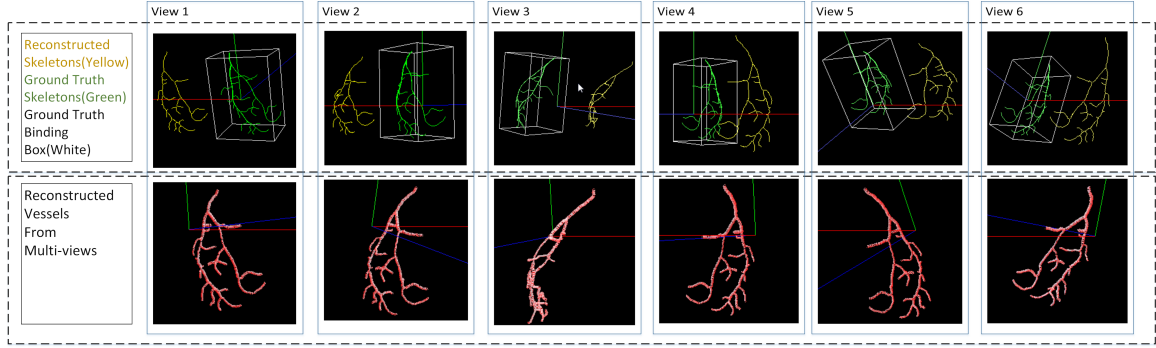


Figure 11: Up: Reconstructed Centerlines and Ground Truth from Different Views; Down: Reconstructed Vessels

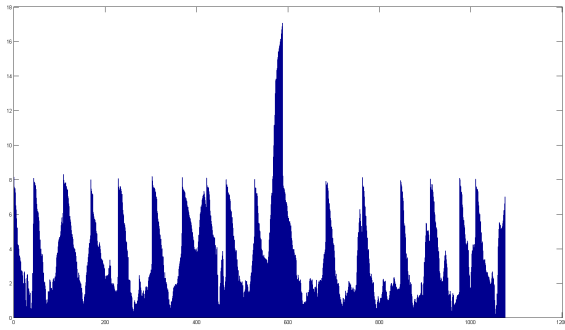


Figure 12: Error Statistics between Reconstructed Skeletons and Ground Truth

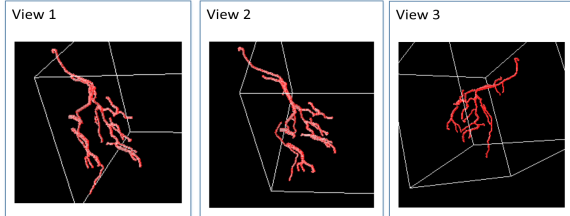


Figure 13: Reconstructed Real Data

of the ground truth. We use the size of the binding box to evaluate the reconstructed skeletons. We compute the distance between each ground truth point and the computed point. Then we compute the average distance as the error. We use the scale the error divides the size of the binding box to evaluate our reconstructed precision.

The error statistics are described as Figure 12.

Finally, we get an average error of 3.833708 and the binding box of (52.691906, 77.026981, 39.552235).

As for the real data, the views and reconstructed data can be found in Figure 13.

| Step | Called Times | Total Time | Average Time |
|------|--------------|------------|--------------|
| 1 | 57 | 66.024s | 1.158s |
| 2 | 30 | 230.634s | 7.6878s |
| 3 | 1 | 27.3s | 27.3s |

Table 1: Step Execution Time

4.2. Performance

Our method consists of three steps and the consuming time of each step can be described in Table 1.

Step 1 indicate Vessel Extraction, step 2 indicate Centerline Tracking and step 3 indicate 3D Reconstruction. According to the table, the centerline tracking and 3D reconstruction step consumes most time, in our future work, we wanna implement them on GPU.

5. Conclusion and Discussion

6. Future Work

We use three projection views to reconstruct the coronary arteries. In our current work, the corresponding image pairs are selected out by hand according to the cardiac cycle. This can be accurate but slow down the reconstruction speed. In the near future, we want to find some method to find the corresponding images automatically. Also, our work is divided into three main parts and the data processing consumes much time, we want to accelerate the image processing step, as well as the reconstruction step with the help of GPU. Finally, we want to build a real-time online reconstruction system.

References

- [1] A. Hoover, V. Kouznetsova, M. Goldbaum, Locating blood vessels in retinal images by piecewise threshold probing of a matched filter response, Medical Imaging, IEEE Transactions on 19 (3) (2000) 203–210.

- 540 [2] Q. Li, J. You, D. Zhang, Vessel segmentation and width estimation
 541 in retinal images using multiscale production of matched
 542 filter responses, *Expert Systems with Applications* 39 (9) (2012)
 543 7600–7610.
- 544 [3] A. F. Frangi, W. J. Niessen, K. L. Vincken, M. A. Viergever,
 545 Multiscale vessel enhancement filtering, in: *Medical Image
 546 Computing and Computer-Assisted InterventionlMICCAI98*,
 547 Springer, 1998, pp. 130–137.
- 548 [4] A.-P. Condurache, T. Aach, Vessel segmentation in angiograms
 549 using hysteresis thresholding, in: *IAPR Conference on Machine
 550 Vision Applications*, Citeseer, 2005.
- 551 [5] A. K. Klein, F. Lee, A. A. Amini, Quantitative coronary angiog-
 552 raphy with deformable spline models, *Medical Imaging, IEEE
 553 Transactions on* 16 (5) (1997) 468–482.
- 554 [6] L. Sarry, J.-Y. Boire, Three-dimensional tracking of coronary
 555 arteries from biplane angiographic sequences using paramet-
 556 rically deformable models, *Medical Imaging, IEEE Transactions
 557 on* 20 (12) (2001) 1341–1351.
- 558 [7] C. Cañero, F. Vilariño, J. Mauri, P. Radeva, Predictive (un) dis-
 559 tortion model and 3-d reconstruction by biplane snakes, *Medical
 560 Imaging, IEEE Transactions on* 21 (9) (2002) 1188–1201.
- 561 [8] S. Park, J. Lee, J. Koo, O. Kwon, S. Hong, Adaptive tracking
 562 algorithm based on direction field using ml estimation in an-
 563 giogram, in: *TENCON'97. IEEE Region 10 Annual Confer-
 564 ence. Speech and Image Technologies for Computing and T-
 565 elecommunications., Proceedings of IEEE*, Vol. 2, IEEE, 1997,
 566 pp. 671–675.
- 567 [9] A. C. Dumay, J. J. Gerbrands, J. H. Reiber, Automated extrac-
 568 tion, labelling and analysis of the coronary vasculature from ar-
 569 teriograms, *The International Journal of Cardiac Imaging* 10 (3)
 570 (1994) 205–215.
- 571 [10] S. R. Aylward, E. Bullitt, Initialization, noise, singularities, and
 572 scale in height ridge traversal for tubular object centerline ex-
 573 traction, *Medical Imaging, IEEE Transactions on* 21 (2) (2002)
 574 61–75.
- 575 [11] A. Sen, L. Lan, K. R. Hoffmann, Improved coronary vessel
 576 tracking using non-linear filter enhanced x-ray angiograms, in:
 577 *Engineering in Medicine and Biology Society, 1997. Proceed-
 578 ings of the 19th Annual International Conference of the IEEE*,
 579 Vol. 2, IEEE, 1997, pp. 573–576.
- 580 [12] A. Sen, L. Lan, K. Doi, K. R. Hoffmann, Quantitative evaluation
 581 of vessel tracking techniques on coronary angiograms, *Medical
 582 Physics* 26 (1999) 698.
- 583 [13] C. Kirbas, F. Quek, A review of vessel extraction techniques and
 584 algorithms, *ACM Computing Surveys (CSUR)* 36 (2) (2004)
 585 81–121.
- 586 [14] E. Wellnhofer, A. Wahle, I. Mugaragu, J. Gross, H. Os-
 587 wald, E. Fleck, Validation of an accurate method for three-
 588 dimensional reconstruction and quantitative assessment of vol-
 589 umes, lengths and diameters of coronary vascular branches and
 590 segments from biplane angiographic projections, *The Interna-
 591 tional Journal of Cardiac Imaging* 15 (5) (1999) 339–353.
- 592 [15] J. C. Messenger, S. J. Chen, J. D. Carroll, J. Burchenal,
 593 K. Kiousopoulos, B. M. Groves, 3d coronary reconstruction
 594 from routine single-plane coronary angiograms: clinical vali-
 595 dation and quantitative analysis of the right coronary artery in 100
 596 patients, *The International Journal of Cardiac Imaging* 16 (6)
 597 (2000) 413–427.
- 598 [16] R. R. Gollapudi, R. Valencia, S. S. Lee, G. B. Wong, P. S.
 599 Teirstein, M. J. Price, Utility of three-dimensional reconstruc-
 600 tion of coronary angiography to guide percutaneous coronary
 601 intervention, *Catheterization and Cardiovascular Interventions*
 602 69 (4) (2007) 479–482.
- 603 [17] B. Movassaghi, V. Rasche, M. Grass, M. A. Viergever, W. J.
 604 Niessen, A quantitative analysis of 3-d coronary modeling from
 605 two or more projection images, *Medical Imaging, IEEE Trans-
 606 actions on* 23 (12) (2004) 1517–1531.
- 607 [18] K. Sprague, M. Drangova, G. Lehmann, P. Slomka, D. Levin,
 608 B. Chow, et al., Coronary x-ray angiographic reconstruction and
 609 image orientation, *Medical physics* 33 (2006) 707.
- 610 [19] E. Hansis, D. Schäfer, O. Dössel, M. Grass, Projection-based
 611 motion compensation for gated coronary artery reconstruction
 612 from rotational x-ray angiograms, *Physics in medicine and biol-
 613 ogy* 53 (14) (2008) 3807.
- 614 [20] T. V. Nguyen, J. Sklansky, Reconstructing the 3-d medial axes
 615 of coronary arteries in single-view cineangiograms, *Medical
 616 Imaging, IEEE Transactions on* 13 (1) (1994) 61–73.
- 617 [21] M. L. Marcus, K. C. Dellperger, Determinants of systolic and
 618 diastolic ventricular function, in: *Cardiac Imaging*, 1991, p. p.
 619 24C38.
- 620 [22] J. A. Fessler, A. Macovski, Object-based 3-d reconstruction of
 621 arterial trees from magnetic resonance angiograms, in: *Medical
 622 Imaging, IEEE Transactions on*, Vol. 10, 1991, p. 25C39.
- 623 [23] I. Liu, Y. Sun, Fully automated reconstruction of three-
 624 dimensional vascular tree structures from two orthogonal views
 625 using computational algorithms and productionrules, *Optical
 626 Engineering* 31 (10) (1992) 2197–2207.
- 627 [24] J. Weng, N. Ahuja, T. S. Huang, Optimal motion and structure
 628 estimation, *Pattern Analysis and Machine Intelligence, IEEE
 629 Transactions on* 15 (9) (1993) 864–884.
- 630 [25] S.-Y. J. Chen, K. R. Hoffmann, J. D. Carroll, Three-dimensional
 631 reconstruction of coronary arterial tree based on biplane an-
 632 giograms, *Proc SPIE Med Imag: Image Processing* 2710 (1996)
 633 103–114.
- 634 [26] S.-Y. J. Chen, C. E. Metz, Improved determination of biplane
 635 imaging geometry from two projection images and its applica-
 636 tion to 3-d reconstruction of coronary arterial trees, in: *Med.
 637 Phys.*, Vol. 24, 1997, p. 633C654.
- 638 [27] G. Finet, J. Lienard, Optimizing coronary angiographic views,
 639 *The International Journal of Cardiac Imaging* 11 (1995) 53–54.
- 640 [28] Y. Sato, T. Araki, M. Hanayama, H. Naito, S. Tamura, A view-
 641 point determination system for stenosis diagnosis and quan-
 642 tification in coronary angiographic image acquisition, *Medical
 643 Imaging, IEEE Transactions on* 17 (1) (1998) 121–137.
- 644 [29] E. E. van der Wall, Whats new in cardiac imaging, in: *Nuclear
 645 Cardiology and Cardiac Magnetic Resonance*, Springer, 1992,
 646 pp. 255–268.
- 647 [30] S. J. Chen, J. D. Carroll, 3-d reconstruction of coronary arterial
 648 tree to optimize angiographic visualization, *Medical Imaging,
 649 IEEE Transactions on* 19 (4) (2000) 318–336.
- 650 [31] E. H. Land, An alternative technique for the computation of the
 651 designator in the retinex theory of color vision, *Proceedings of
 652 the National Academy of Sciences* 83 (10) (1986) 3078–3080.
- 653 [32] D. J. Jobson, Z.-u. Rahman, G. A. Woodell, Properties and per-
 654 formance of a center/surround retinex, *Image Processing, IEEE
 655 Transactions on* 6 (3) (1997) 451–462.
- 656 [33] A. Moore, J. Allman, R. M. Goodman, A real-time neural sys-
 657 tem for color constancy, *Neural Networks, IEEE Transactions
 658 on* 2 (2) (1991) 237–247.
- 659 [34] A. Hurlbert, Formal connections between lightness algorithms,
 660 *JOSA A* 3 (10) (1986) 1684–1693.
- 661 [35] M. S. Hassouna, A. A. Farag, Multistencils fast marching meth-
 662 ods: A highly accurate solution to the eikonal equation on car-
 663 tesian domains, *Pattern Analysis and Machine Intelligence, IEEE
 664 Transactions on* 29 (9) (2007) 1563–1574.
- 665 [36] J. A. Bærentzen, On the implementation of fast marching meth-
 666 ods for 3d lattices, *Tech. rep.* (2001).